ELSEVIER

Mechanical Properties of the Aggregate and Cement Interface

Matthew J. Aquino, Zongjin Li, and Surendra P. Shah
ACBM Center, Northwestern University, Evanston, Illinois

The interface between aggregate and cement based matrices plays an important role in determining the properties of concrete. In an earlier study, a push-out test technique and a theoretical model were proposed to determine the stiffness, strength, and surface energy of the interface layer. To be valid material properties, these bond parameters should be independent of the geometry of the specimen, and this was confirmed in this study. The influence of neighboring sand and aggregate particles on the bond properties of the push-out aggregate was analyzed and found to be quite small. On the other hand, the addition of polymer latex and silica fume had major effects on the bond properties. All tests were performed in a closed-loop manner to obtain the load versus slip relationship. The microstructure of the interfacial zone was investigated with the use of backscattered electron imaging. ADVANCED CEMENT BASED MATERIALS 1995, 2, 211–223

KEY WORDS: Aggregate, Debonding, Fracture, Interface, Latex, Microstructure, Push-out, Silica fume, Surface energy

There are many factors associated with the strength and the durability of concrete. One area of particular interest is the interfacial zone between cement paste and aggregate. Researchers have investigated the chemical and the mechanical properties of the interfacial zone as well as the morphology of the hydration products at the cement paste/aggregate interface [1–11]. Due to the high porosity found at the interfacial zone, the aggregate-cement bond is considered to be the weak link in the concrete composite with normal compressive strength.

In a study reported earlier [12], a push-out test was developed to obtain the load-slip relationship of the interface. Based on the observed load-slip relationship and a one-dimensional shear-lag model, material parameters to characterize the interfacial zone were proposed. These parameters included the stiffness of the interfacial zone, the shear and frictional bond strengths, and the interfacial fracture energy. A good correlation was indicated between the values of these bond parameters and the microstructure of the interface.

The aforementioned experiments were performed on a single-size cylindrical aggregate that was pushed out from a surrounding annulus of a cement paste matrix. If the bond parameters determined from the load versus slip curves are to be considered as valid material parameters, then they should be independent of the dimension of the test specimens. One of the goals of the study reported in this paper is to examine the influence of the diameter and the embedment length of the aggregate core on the values of the bond parameters.

The properties of the aggregate-cement interfacial zone may be influenced by the presence of the neighboring aggregates. To examine this influence, tests were carried out when the pushed-out aggregate cylinder was surrounded by pure cement paste, cement paste with sand particles, or cement paste with other coarse aggregates. The effects of the addition of polymer latex and silica fume to the cement paste mixture were also studied.

Tests were conducted in a closed-loop manner to obtain the load-slip relationship. Results were analyzed using a theoretical model. The study also included the use of backscattered electron image for a microstructural investigation of the interfacial zone.

Experimental Details for Mechanical Test and Microscopic Study

Specimen Preparation and Test Setup for Mechanical Test

Indiana limestone, cored out of a stone block using diamond-edged drill bits, was the aggregate used in all tests. Three core diameters were used: 12 mm (0.46 inch), 18 mm (0.72 inch) and 28 mm (1.12 inches). The surface of the aggregate was not pretreated in any experiments. Plastic cylindrical molds were used with dimensions $D_a/D_m = 0.23$, where D_a is the diameter of the aggregate and D_m is the diameter of the mold. The

Address correspondence to: Surendra P. Shah, NSF Center for Advanced Cement Based Material, Northwestern University, Department of Civil Engineering, 2145 Sheridan Road, Room A130, Evanston, IL 60201.
Received June 24, 1994; Accepted January 25, 1995

ISSN 1065-7355/95/$9.50
SSDI 1065-7355(95)00019-N

Adv Cem Bas Mat
1995;2:211–223

dimensions of various test specimens are indicated in Figure 1.

ASTM Type I portland cement with a constant water:cement ratio of 0.35 was used throughout all experiments. The aggregate core was first inserted in the molds and then the molds were filled with the cement paste matrix and vibrated on the vibrating table. The specimens were allowed to cure for 24 hours and then removed from the molds and cured in water for 28 days at a temperature of 20°C (68°F). After curing, the specimens were sliced, perpendicular to the core, into an appropriate thickness and ground and polished on both top and bottom surfaces before testing. The top and bottom surfaces needed to be flat and parallel to ensure that the specimens lie completely flat on the loading fixture. It should be noted that the reference specimens as well as the specimens tested to study the influence of additives and restraining aggregates had an aggregate with a diameter of 12 mm (0.46 inch) and an embedded length of 13 mm (0.50 inch) (specimen type 1–6, Table 1).

The test apparatus setup is shown in Figure 2. The specimen was placed on a flat circular plate that was connected to a servohydraulic actuator of a MTS machine through a hollow cylinder. The entire specimen/fixture could move up with the actuator. The steel rod, connected to the load cell, made contact with the top surface of the aggregate. Resistance provided by the

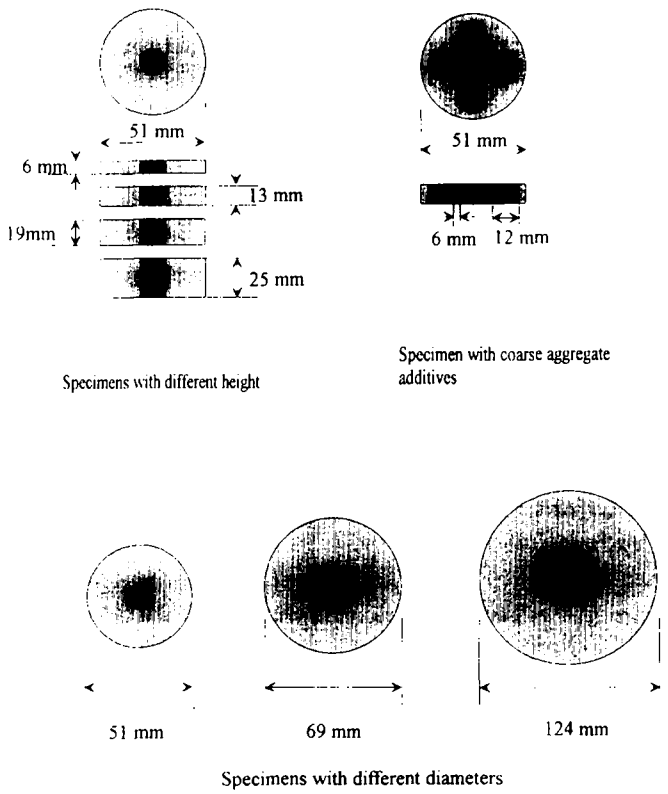

FIGURE 1. Dimensions of various test specimens.

TABLE 1. Experimental test program

Specimen Type*	Curing Age (days)	Cement Matrix Additives (w:c = 0.35)	Aggregate Core Dimensions: Diameter (mm)	Aggregate Core Dimensions: Embedded Length (mm)
1	28	None (reference)	12	13
2	28	Silica fume	12	13
3	28	Latex	12	13
4	28	Latex + antifoamer	12	13
5	28	Coarse aggregate	12	13
6	28	Fine aggregate	12	13
7	28	None	12	6
8	28	None	12	18
9	28	None	12	25
10	28	None	18	13
11	28	None	28	13

*For each type of specimen, three identical specimens were tested.

upward movement of the loading fixture pushed the cylindrical aggregate core downwards. Two linear variable differential transformers (LVDTs), which were fixed between the specimen and the rigid wing of the steel rod, were used to measure slip displacement at the top of the aggregate relative to the surface of the cement matrix annulus. The average output of the LVDTs was used as a feedback signal to control the servohydraulic system. The rate of slip displacement of the push-out test was about 1 mm/hour. Slip displacement of the bottom of the aggregate was measured by an additional LVDT. Push-out load, slip displacement

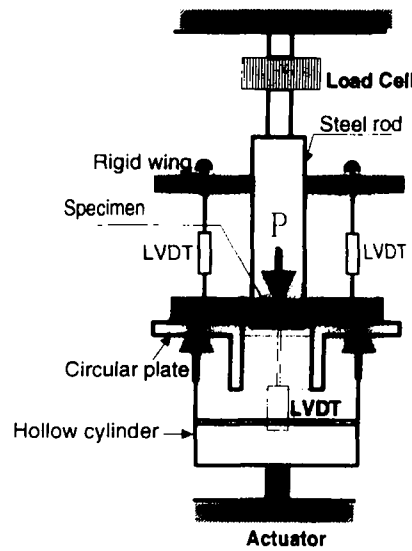

FIGURE 2. Push-out test set-up.

of aggregate, and stroke of the actuator of MTS were recorded using a data acquisition computer.

Specimen Preparation for Microscopic Study

Specimens were cast in the same manner as previously discussed using the same compositions to enable a comparison with the result of the push-out tests. After curing for 28 days, the samples were sliced perpendicular to the axis of the cored aggregate to a thickness of approximately 1 mm using a diamond saw.

The sliced specimens were placed in ethanol to stop hydration until they were ready to be prepared for examination. The specimens were placed in a vacuum to remove all moisture and foreign substances from the surface and were impregnated with a low viscosity epoxy while under the vacuum. The samples were then removed from the vacuum chamber and allowed to cure for 24 hours with the addition of a hardening accelerator. After curing, the specimens were sanded and polished for a clear examination. They were first dry polished with 320 grit sandpaper followed by a 400 grit sandpaper to remove the hardened epoxy from the specimen surface. Next, they were wet polished using a 600 gritsand paper and a nonaqueous polishing lubricant. Finally, to remove all scratches formed by the sandpaper, lapp cloths impregnated with diamond pastes of 3 μm and 1 μm were used for the final polish.

Mechanical Experimental Data Analysis

For a typical push-out test, the measurements of importance are push-out load, displacements at the top of the aggregate, and slip displacement at the bottom of the aggregate. Figure 3 shows two curves of slip displacement superimposed over the push-out loading curve as a function of time. The displacement at the top of the aggregate is represented by a single line while the curve of the slip displacement at the bottom of the aggregate is composed of three ascending stages. The first portion of the curve reflects the elastic deformation of the aggregate and the interfacial zone. The steeper slope in the second portion implies that the deformation rate is increased. This means that the interfacial zone became less stiff, perhaps due to breaking of elastic bonds. Hence, the end point of the first portion marks the initial debonding, and the second

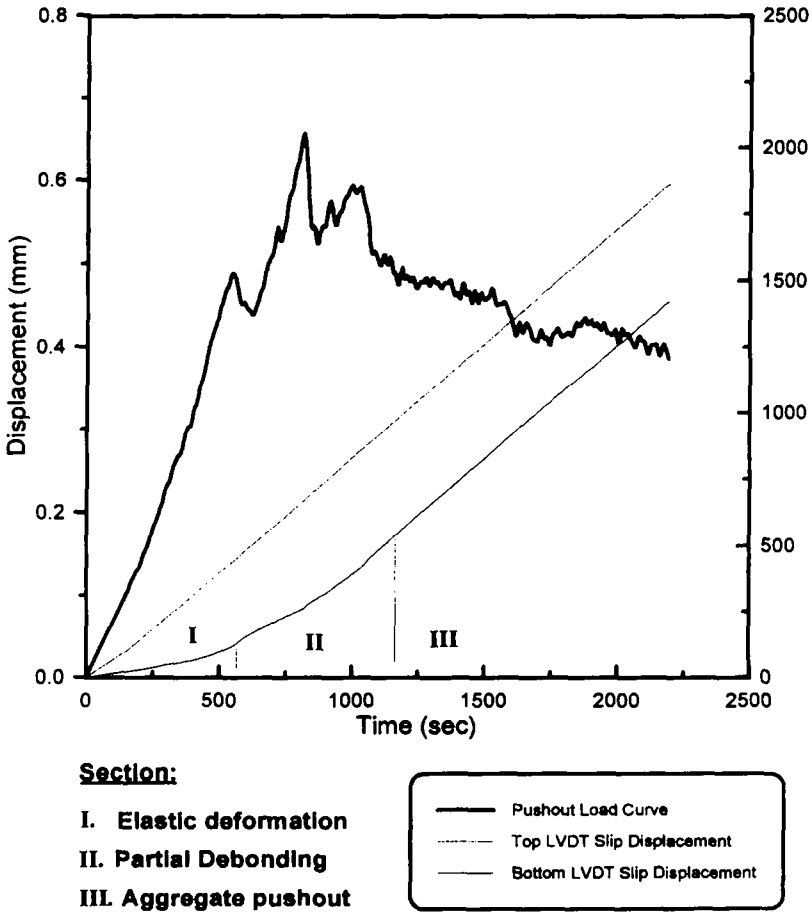

FIGURE 3. Displacement and push-out load curves as a function of time, showing three stages of loading process.

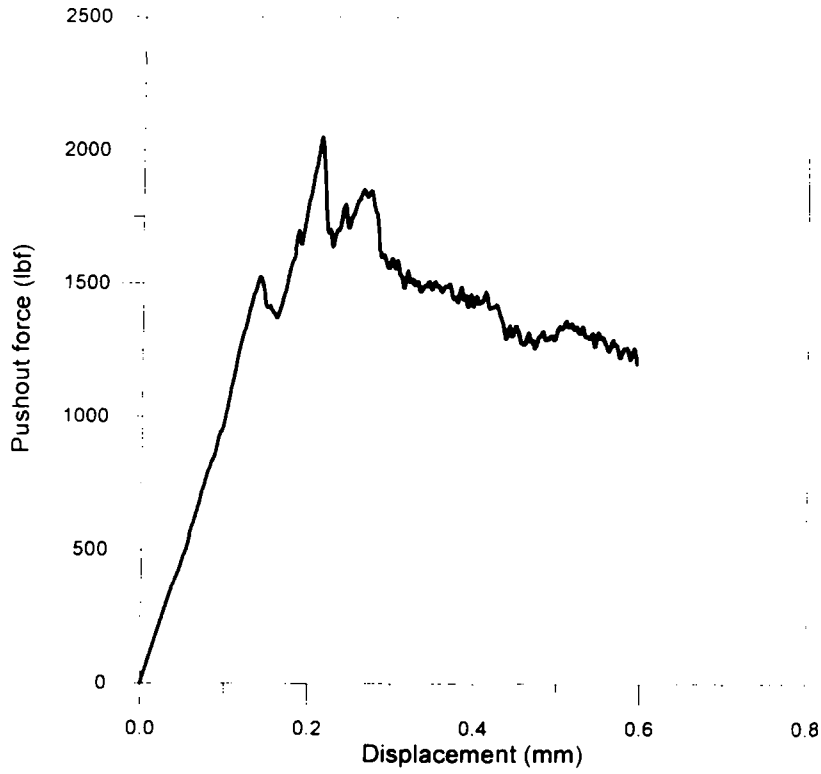

FIGURE 4. Push-out load curve as a function of displacement measured at the top of the specimen.

portion of the curve could be called a partial debonding stage. The point at which the top and bottom measured displacement become parallel signals the start of the third stage. During this stage, the top of the aggregate and the bottom of the aggregate undergo the same amount of incremental displacement. This corresponds to complete debonding. It should be noted that complete debonding of the interface occurs after peak load has been achieved as can be seen from the push-out load curve.

A typical push-out load versus slip displacement curve (the average of the two top LVDTs) is shown in Figure 4. From such plots, the following parameters were determined: the peak load, displacement at peak load, and the slope of linear elastic stage. From these values and using the analysis described later, the interface stiffness parameter, ω, interfacial frictional strength, τ_f, interfacial bond strength, τ_y, and interfacial specific surface energy, Γ, can be obtained. It should be noted that sometimes several peaks and valleys were observed before a gradual descending stage was reached. In this case, the top and bottom slip displacements (as in Figure 3) were helpful in determining when the complete debonding took place.

To obtain the characteristic properties of the interface from the load-slip curve, a mathematical model [13], in which the fracture concepts have been taken into account, was used. A brief summary of this theoretical model is given below (see Figure 5). In Figure 5, L represents the aggregate embedded length. The aggregate is assumed to be elastic with Young's modulus of E_a and cross-sectional area A. The bulk matrix is assumed to be rigid except for the interfacial layer that is idealized as an elastoplastic shear layer.

It is assumed that debonding has occurred over a certain length, a, starting at $x = L$. Treating the boundary layer as a shear lag and assuming that a constant shear stress is acting at the debonded interface, one can write the following equations:

$$q = \begin{bmatrix} kU(x) & 0 < x < L - a \\ q_f & L - a < x < L \end{bmatrix} \quad (1)$$

where k is the stiffness per unit length of the interfacial

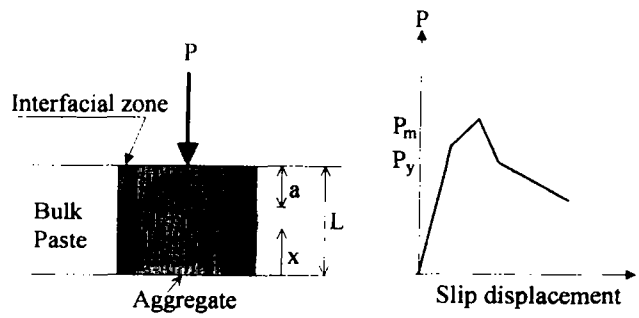

FIGURE 5. Parameters for the mathematical model for aggregate push-out test. P = aggregate push-out force; L = aggregate embedded length.

layer for small deformation, q is the shear force per unit length acting on the aggregate, q_f is the frictional shear force per unit length, and $U(x)$ is the aggregate displacement.

Denoting the aggregate push-out force as P, the equilibrium equation and the constitutive relationship for the aggregate can be written as:

$$\frac{dP}{dx} - q = 0 \tag{2}$$

$$\frac{P}{A} = E_a \frac{dU}{dx} \tag{3}$$

Introducing eqs 1 and 3 into eq 2, the following differential equation for U can be obtained,

$$\begin{aligned} U_{,xx} - \omega^2 U &= 0 \quad 0 < x < (L - a) \\ U_{,xx} - \frac{q_f}{E_a A} &= 0 \quad (L - a) < x < L \end{aligned} \tag{4}$$

in which the subscript comma "," indicates differentiation. The quantity ω is defined as:

$$\omega = \sqrt{\frac{k}{E_a A}} \tag{5}$$

Equations 4, together with boundary conditions and continuity conditions, constitute a complete set of equations for the determination of $U(x)$. Solving this set of equations, the following closed form expression for the slip displacement at the loading end, U^*, is obtained:

$$U^* = U(L) = \frac{P^* - q_f a}{E_a A \omega} \coth(\omega (L - a)) + \frac{P^* - 0.5 q_f a}{E_a A} a \tag{6}$$

The relationship between U and P in the elastic stage can be obtained from eq 6 by setting $a = 0$. This leads to

$$\frac{P^*}{U^*} = E_a A \omega \tanh[\omega(L)] \tag{7}$$

The stiffness parameter ω can be determined from the initial slope of the experimental load-slip displacement curves for a push-out test using eq 7 [14].

Furthermore, it is shown [13] that the relationship between the push-out force and debonding length, a, can be derived either from the shear strength (q_y) criterion (material properties represented by q_y, and q_f) or from the fracture energy (Γ) criterion (material properties represented by Γ, and q_f). For the shear strength (q_y) criterion, the derivation is obtained from overall equilibrium of the forces acting on aggregate. For the fracture energy criterion, a differential equation for P is first derived by applying the energy balance concept, and then the expression for P is obtained by solving the differential equation. The expressions for P take the following forms:

for the shear strength criterion,

$$P^* = q_f a + \frac{q_y \tanh\omega(L - a)}{\omega}, \tag{8}$$

and for the fracture energy criterion,

$$P^* = q_f a + \left[\frac{q_f}{2\omega} + \sqrt{\left(\frac{q_f}{2\omega}\right) + 2E_a A\, p\, \Gamma}\right] \tanh(\omega(L - a)) \tag{9}$$

in which Γ is the specific fracture energy.

Note that three material parameters are needed for either model. They are ω, q_y, and q_f or ω, Γ, and q_f.

To determine the interfacial yield parameter, q_y, the interfacial frictional forces, q_f, and the specific energy, Γ, one needs to know the length of debonded crack, a, at the peak load. A method that utilizes the maximum load, P^*_{max}, and the slip displacement corresponding to P^*_{max} was used [14]. The formula used to calculate q_f, q_y, and Γ are eqs 10, 11, and 12, respectively,

$$q_f = \frac{\omega P^*_{max}}{a\omega + \sinh(\omega(L - a))\cosh(\omega(L - a))} \tag{10}$$

$$q_y = q_f \cosh^2(\omega(L - a)) \tag{11}$$

$$2E_a A\Gamma = \left(\frac{q_f}{2\text{IIR}\omega}\right)^2 [\cosh^4(\omega(L - a)) - \cosh^2(\omega(L - a))] \tag{12}$$

Note that an additional equation (eq 13) is needed to determine the debonding length, a.

$$P^*_{max} \frac{0.5(\omega a)^2 + \cosh^2(\omega(L - a)) + \omega a \sinh(\omega(L - a))\cosh(\omega(L - a))}{\omega a + \sinh(\omega(L - a))\cosh(\omega(L - a))} - U^*_{peak} E_{aA} \omega = 0 \tag{13}$$

Microstructure Analysis

The aggregate/cement interfacial zone was examined on a microscopic level through the backscatter mode of a scanning electron microscope (SEM) with an energy dispersive X-ray analysis system (EDAX). Based on previous work [3], an image magnification of 400× was selected for the analysis. Each region of different brightness in the images had been previously analyzed with the EDAX analysis system to identify the chemical components incorporated into the interface. These components can include calcium hydrosilicate (C-S-H), calcium hydroxide, unhydrated cement (anhydrous phase), and pores [12,15].

It has been found that the grey level in the SEM images could be used to identify phases in the microstructure. The two most important phases of interest are the anhydrous and the porous phases that are at opposite ends of the grey spectrum. In the SEM images, the porous phase is represented by the dark region while the anhydrous phase is represented by the bright (white) region. Through a close examination of the micrographics, one can gain an idea of the amount of porosity contained at the aggregate/cement interface.

Using conventional Polaroid micrographs taken from the SEM, a quantitative analysis of the aggregate/cement interface was performed. The micrographs were digitized by a video camera attached to a Tracor-Northern 8500 image analysis system. The binary images were constructed by determining a grey level threshold value that appears to segment the porosity from the other hydration product. The grey level thresholds were selected by the operator's judgment that has been satisfactory in providing reasonably good results. The final digitized binary images were 512 × 512 pixels that resulted in approximately 0.5 microns per pixel at a resolution of 400× [12].

For each digitized image, the interfacial zone was divided into segmental bands 20 μm in width up to 120 μm from the aggregate surface. The digitized binary images of each segmental band were analyzed to determine the area percentage of pore space. By plotting the average area percentage versus the distance from the aggregate surface, we established gradient plots for the aggregate/cement interface for each image.

Results

Mechanical Test Results

The results of the push-out test can be arranged into two groups that will be discussed separately. The groups are (1) effect of aggregate size and (2) effect of variations in cement paste composition.

EFFECT OF AGGREGATE SURFACE AREA. In this set of experiments, the varied surface areas were obtained by either changing aggregate embedded lengths (6, 13, 18, or 25 mm) with a fixed diameter (12 mm) or using different diameters of 12, 18, or 25 mm with a fixed embedded length (13 mm). Figures 6 to 9 are the compilation of the calculated bond parameters and properties plotted against the aggregate surface area. In Figure 6, the interfacial stiffness parameter (ω) is plotted versus bond surface area for two sets of specimen. One set of results was obtained by varying the aggregate embedded length, whereas the other set of results was obtained by varying the aggregate diameter. The graph indicates that the interfacial stiffness parameter is essentially independent of the embedment length or the diameter of the aggregate. A similar trend can be seen

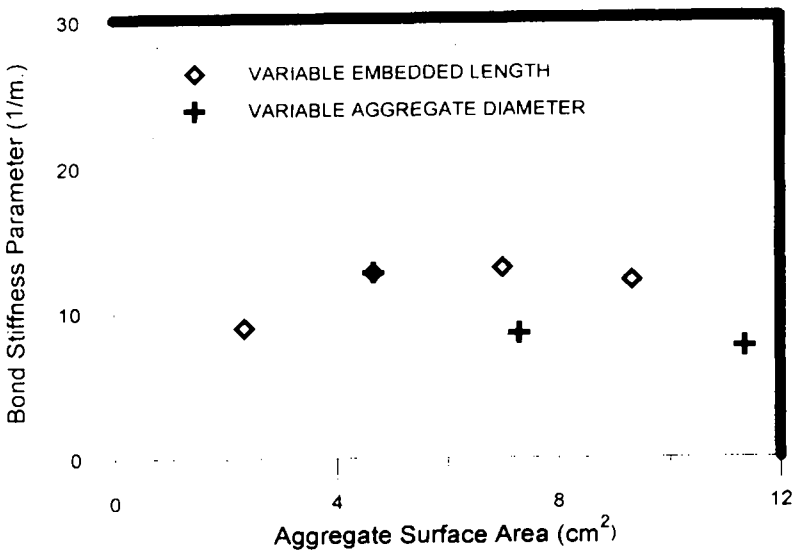

FIGURE 6. The interfacial stiffness parameter as a function of aggregate surface area.

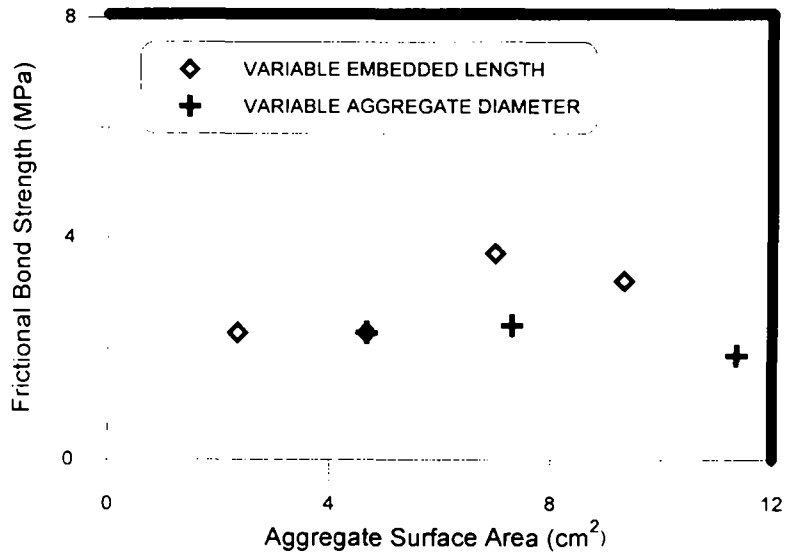

FIGURE 7. The frictional bond strength as a function of aggregate surface area.

from Figures 7 and 8, which show that the shear and frictional bond strengths are more or less of the same magnitude for the aggregates with different surface areas. Overall, it seems that these three parameters generally reflect the nature of the aggregate/cement interface properties, because all three variables remained independent of the geometry of the specimen.

Specific surface energy is plotted against the bond surface area in Figure 9. In this case, specimens with increasing embedded length showed an increase in specific surface energy while specimens with increasing diameters stayed constant with specific surface energy. The observed influence of the embedment length of the aggregate on fracture energy can perhaps be explained by the *R*-curve concept. According to the energy concept in fracture mechanics, a crack propagates when the rate of change of strain energy release (G) is equal to the rate of energy consumption (R). G is often called the crack driving force, and R is termed the fracture resistance. The rate referred to is with respect to crack extension. For the push-out specimen, crack length is the length of the debonded zone, a, as shown in Figure 5. For perfectly brittle materials, when $G = R$, a crack catastrophically propagates. However, in quasibrittle materials, the crack steadily propagates until a second condition is also satisfied

$$\frac{\partial G}{\partial a} = \frac{\partial R}{\partial a} \tag{14}$$

For quasibrittle crack propagation, the fracture resistance or *R*-curve is rising as depicted in Figure 10. It was shown by Ouyang et al. [15] that specimens with

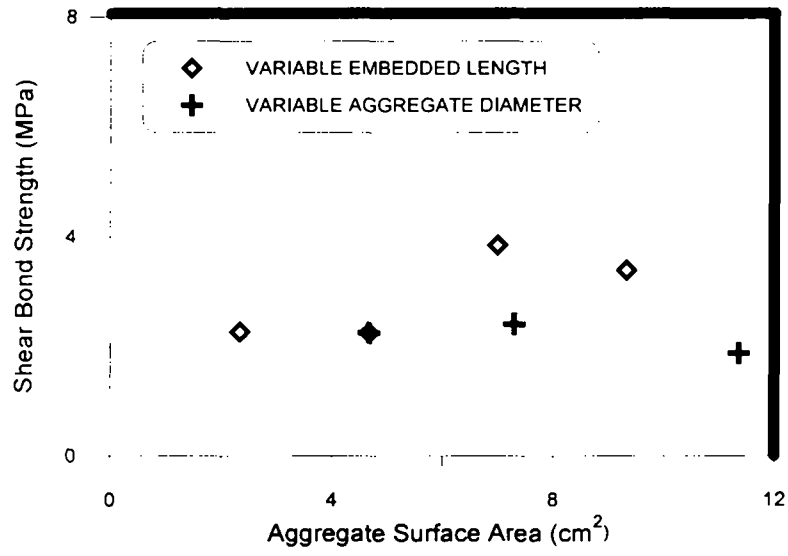

FIGURE 8. The bond shear strength as a function of aggregate surface area.

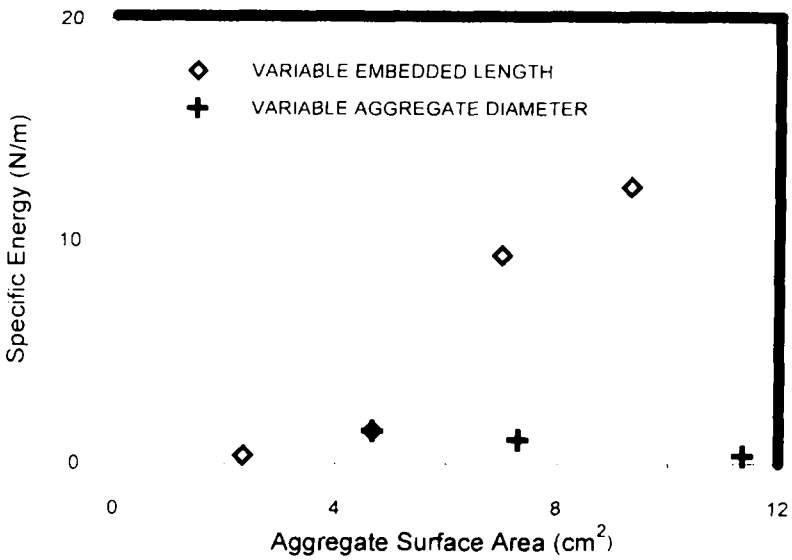

FIGURE 9. The specific surface energy as a function of aggregate surface area.

different embedment lengths have different G curves. Thus the critical point when eq 14 is satisfied is different for different embedment lengths. This may explain why the bond fracture energy calculated assuming a perfectly brittle crack propagation gave different values for aggregates with different embedded lengths.

EFFECTS OF VARIATION IN CEMENT PASTE COMPOSITION. In this phase of the study, the effects of three admixtures—silica fume, latex, and latex with an antifoaming agent—were examined. In addition, effects of fine aggregate (sand with maximum size of 3 mm) and coarse aggregate (four additional aggregate cores of the same diameter of 12 mm) were also analyzed. Bond parameters were calculated using the theoretical model. The results of these tests are listed in Table 2.

The variations to the cement paste were made through the addition of coarse aggregates or sand to the matrix. In the first group of push-out tests for this set, coarse aggregates were added to the specimen to model the interaction of large aggregates on the interfacial bond. The specimens were cast with one center aggregate core surrounded symmetrically by four other aggregate cores of the same material and geometry. The shortest distance between the center aggregate and the four surrounding aggregates was 6 mm. This distance was found to be the average distance separating the coarse aggregates in a typical structural concrete mix. It can be seen from Table 2 that the interfacial properties for these multiple aggregate specimens are lower than those for the reference specimen. Specifically, the specific surface energy decreased by approximately 50%, whereas the shear and frictional bond strengths decreased by about 30%. It appears that additional coarse aggregates may influence the specimen integrity by changing the continuity of the paste. The specimen showed cracks from the push-out loading that propagated through the interface of the additional coarse aggregates. This, in effect, decreased the confining pressure on the pushed aggregate, causing a reduction in interfacial frictional stress. In the second group of push-out tests of this set, sand was added to the cement paste with a sand:cement ratio by weight of 1.5:1. Overall, the addition of sand to the matrix had very little effect on the mechanical properties of the interfacial bond between cement and aggregate. The values of specific surface energy, shear strength, and frictional strength are very close to the values of the reference matrix as shown in Table 2. From these results, it appears that the addition of sand has no effect on the aggregate/cement interfacial bond.

The second set of variations to the reference matrix was made through the addition of admixtures. The first admixture used in the present study was a carboxylated styrene-butadiene copolymer latex. (Tylac ® 97314-00, Emulsion Polymers Division, Reichhold Chemicals, Inc., Dover, DE, July 1989). It has been shown that the addition of this latex to cement paste improves adhesion, resistance to permeability, abrasion resistance, freeze-thaw resistance, flexural strength, and tensile strength. When mixed with the

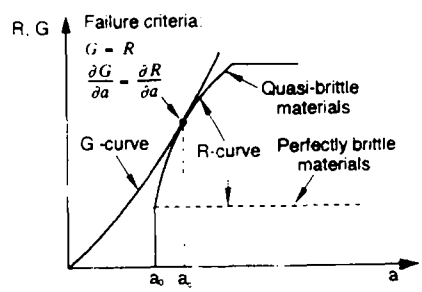

FIGURE 10. R- and G-curves for brittle and quasibrittle materials. a = length of the debonded zone.

TABLE 2. Test results for specimens with different additives

Specimen Type	Interface Stiffness Parameter (ω [l/m])	Interfacial Bond Strength (τ_y [MPa])	Interfacial Frictional Strength (τ_f [MPa])	Interfacial Specific Surface Energy (Γ (N/m])
Reference (plain matrix) specimen	12.80	2.28	2.26	1.40
Coarse aggregate additive	10.20	1.62	1.60	0.70
Sand additive matrix	11.46	2.16	2.13	1.21
Latex additive matrix	10.71	2.70	2.67	2.08
Latex and antifoamer additive matrix	14.92	3.70	3.63	3.81
Silica fume additive matrix	13.19	4.79	4.71	6.59

portland cement, the latex forms a "comatrix" composed of hydrated portland cement paste and coalesced polymer film. The comatrix effectively binds the aggregates together and binds the mix to nonplastic, nonoily, or nondusty surfaces. In addition, many of the microcracks and pores formed in hydrated cement paste are "bridged" by the coalesced polymer film. A side effect of the addition of latex to the cement paste is an increase of air entrainment in the cement matrix. It has also been shown that the latex will act as a water-reducing agent. This may be responsible for some of the improved cement properties and characteristics.

The latex copolymer (emulsion) was added in a latex:cement ratio of 1:2 (by mass) that was recommended by the latex manufacturer. Overall, the results obtained through the push-out test seemed to confirm the improved aggregate-to-cement bonding properties stated earlier. As shown in Table 2, increases in the shear and frictional bond strengths were about 20% over the reference cement. On the other hand, the increase in specific surface energy of the interfacial bond was in the range of 50%.

In addition to the latex-modified cement matrix, a combination of latex plus an antifoaming agent (1% by mass of cement) was added to the cement paste for the

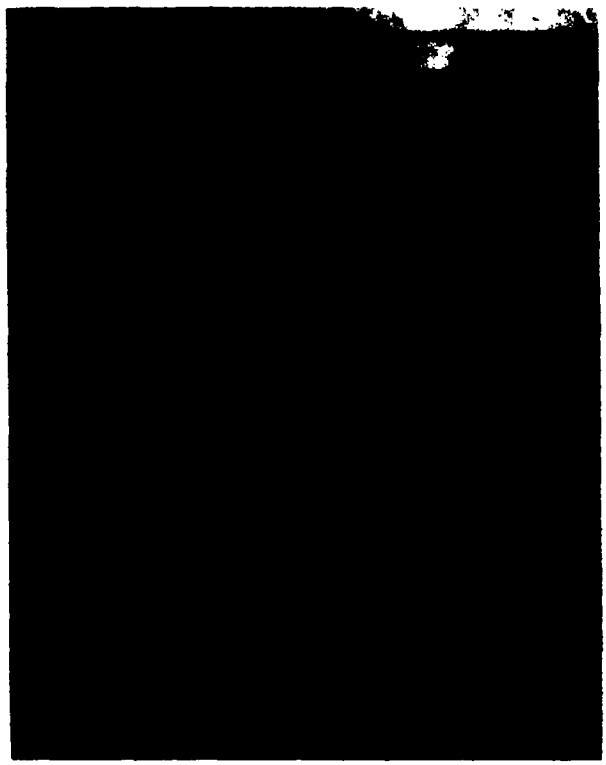

FIGURE 11. SEM micrograph of the aggregate-cement interface for reference specimen.

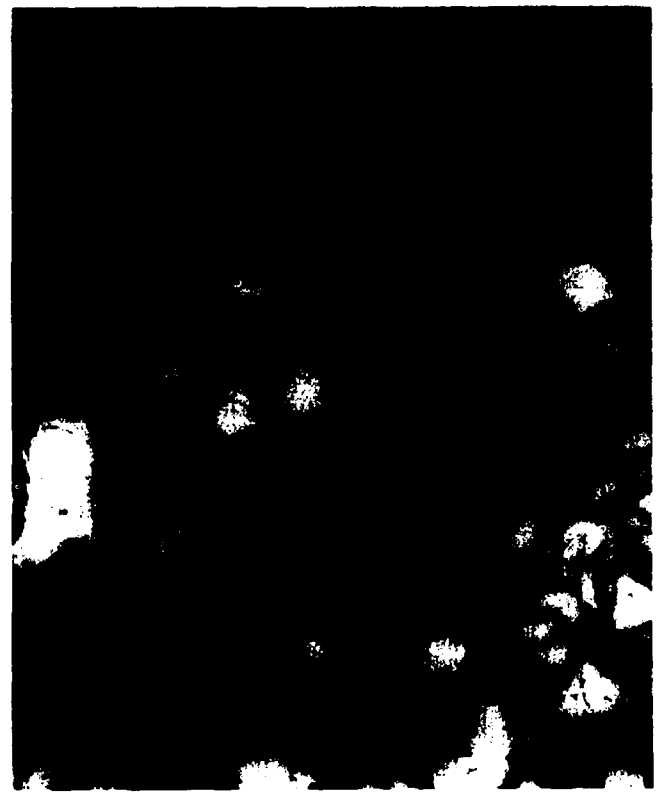

FIGURE 12. SEM micrograph of the aggregate-cement interface for the specimen with sand additive.

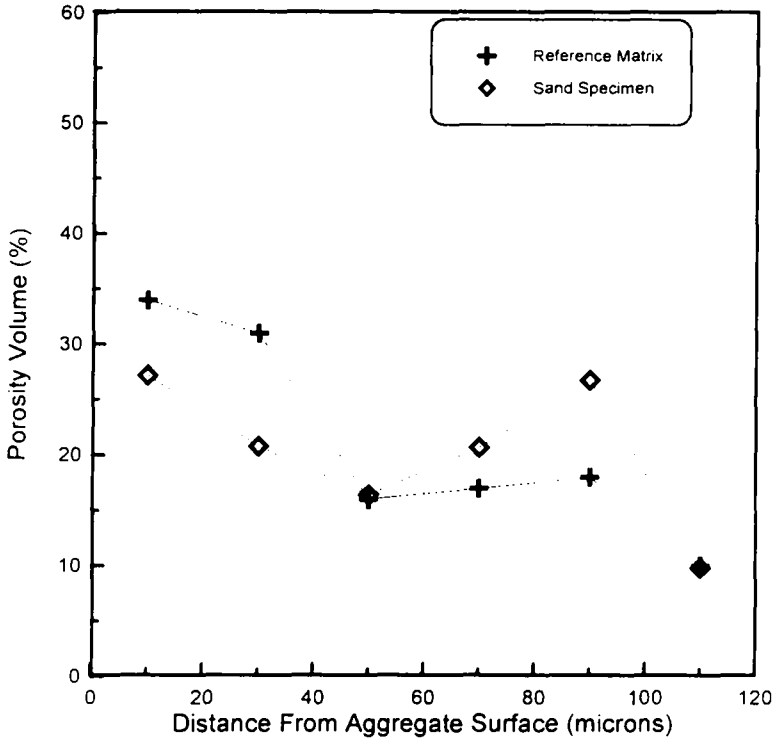

FIGURE 13. Porosity gradient plots for reference specimen and sand-modified specimen.

study. The antifoaming agent was added to decrease the volume of voids produced by the latex addition.

Adding the antifoaming agent to the cement matrix proved to be valuable in further improving the interfacial bond characteristics. An increase in the specific surface energy was obtained with a magnitude of almost threefold over the reference specimen and with an increase of 80% over the latex-modified specimen. The increases in shear and frictional bond strengths were observed to be in the range of 60% over the reference specimen and about 35% over the latex-modified specimen as can be seen in Table 2.

The third admixture used in this study was silica fume. In the tested silica fume-modified matrix, 10% by weight of cement was replaced with silica fume. As shown in Table 2, the specific surface energy was almost 5 times greater for the silica fume matrix specimen compared to the reference specimen. The frictional and shear bond strengths were also over twice as large as compared to the reference specimen.

These improvements in bond strength due to the addition of silica fume can be attributed to several factors [16]. First of all, the smaller particle size of silica fume as compared to cement results in a denser interfacial zone due to improved "packing" effect. Secondly, a pozzolanic reaction between the silica fume and calcium hydroxide in cement increases the structure density. A large decrease in porosity at the interface is also observed with the silica fume-modified matrix as a result of the previously mentioned improve-

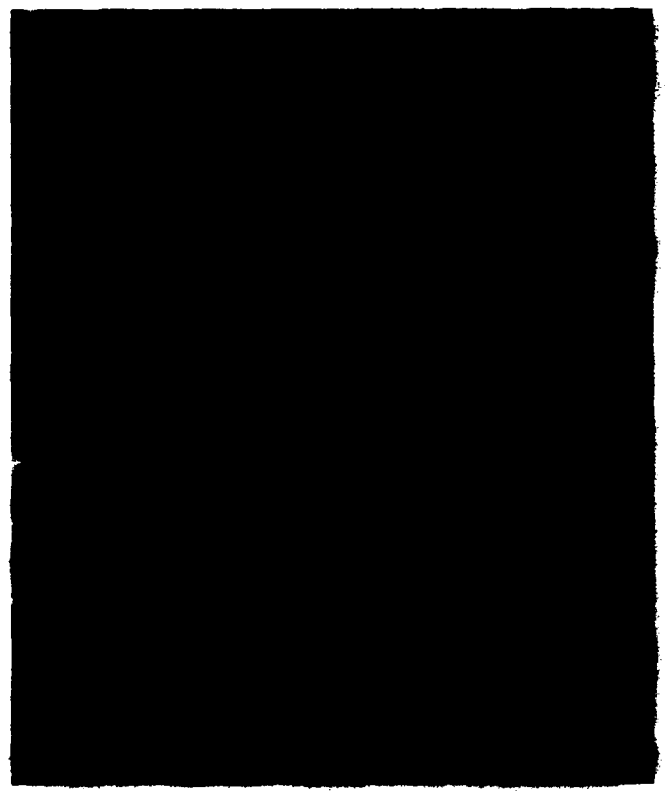

FIGURE 14. SEM micrograph of the aggregate-cement interface for the specimen with latex and antifoaming agent additive.

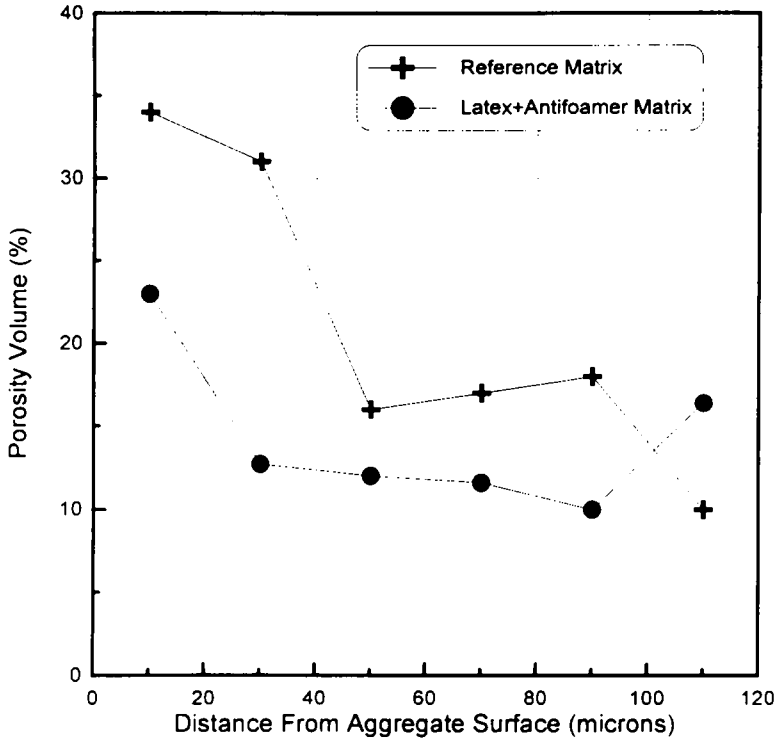

FIGURE 15. Porosity gradient plots for reference specimen and latex and antifoaming agent modified specimen.

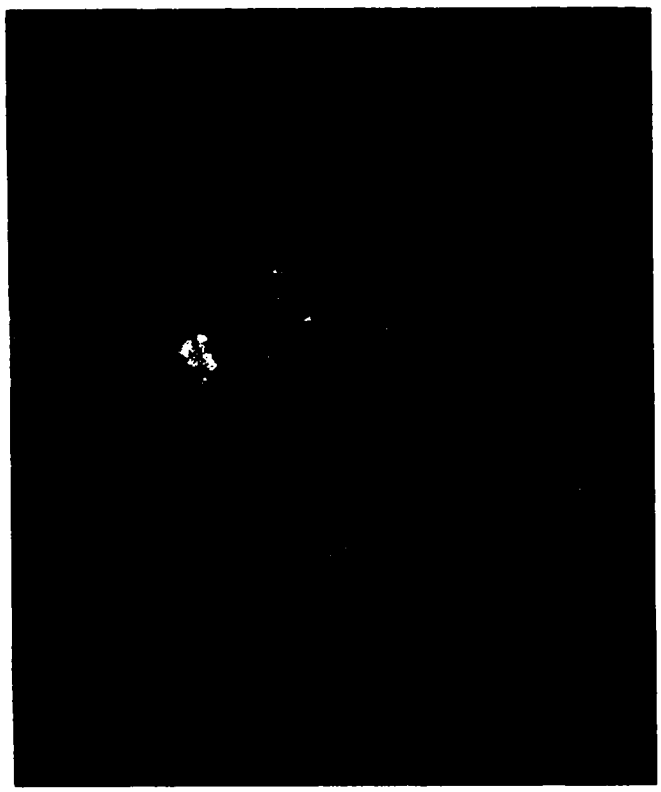

FIGURE 16. SEM micrograph of the aggregate-cement interface for the specimen with silica fume additive.

ments in interfacial density. It has been shown that a more porous interfacial zone and microstructure leads to lower bond strength and surface energy.

Microscopic Evaluation of the Aggregate/Cement Interfacial Zone

Figures 11 and 12 depict SEM photographs of the aggregate/cement interfacial zone. Figure 11 shows the interface of a reference specimen with a clearly visible transition zone. The specimens for which the matrix was modified with sand (Figure 12) show a similar interfacial zone to the reference specimen; this is consistent with their similar mechanical bond properties. The porosity gradient graph (Figure 13) confirms the similarity of the interfacial zone in the sand and the reference specimens.

On the other hand, the SEM photographs of the specimens made with latex and antifoaming agent (Figure 14) showed a decrease in interfacial zone porosity. From the porosity gradient graph (Figure 15), it can be observed that the addition of latex and antifoaming agent resulted in a decrease in porosity of about 40% as compared to the reference specimen. The noted decrease in interfacial porosity is consistent with the separately observed improved mechanical bond properties.

Figure 16 shows an aggregate/cement interface from a specimen of silica fume-modified matrix. In this case,

Advn Cem Bas Mat
1995;2:211-223

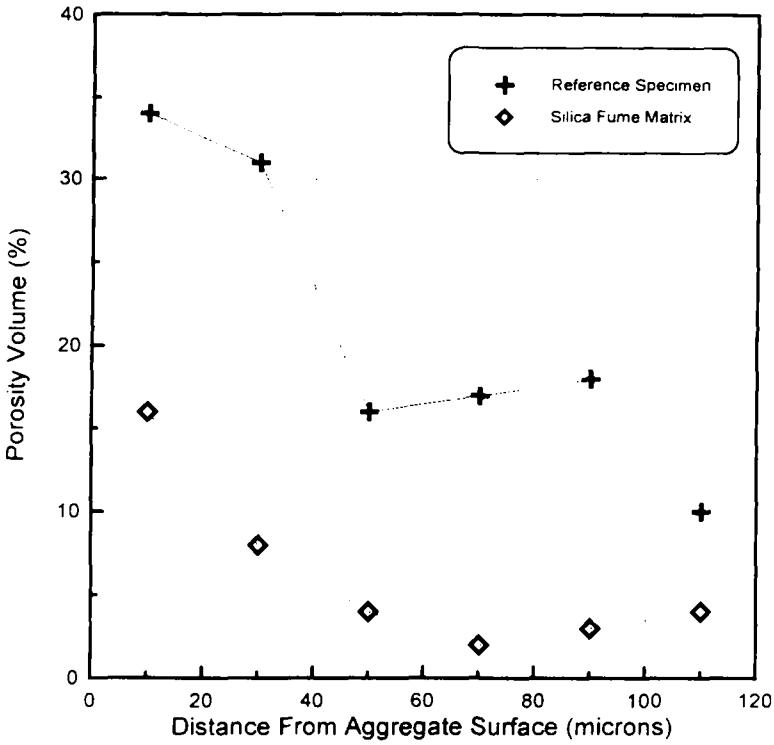

FIGURE 17. Porosity gradient plots for reference specimen and silica fume-modified specimen.

the porous region is almost eliminated. Figure 17 is a porosity gradient graph taken from the results of the image analysis study of SEM photographs of the aggregate/cement interface. The graph shows an average decrease in porosity for the silica fume specimen of about 60% throughout the interface as compared to the reference specimen. These results offer a likely explanation for the improved mechanical bond properties obtained from the push-out test results.

Conclusion

Using a newly developed push-out test method, a load-slip relationship was obtained for the aggregate/cement bond. Given the load-slip displacement curve, the mechanical bond parameters such as interfacial stiffness, shear bond strength, frictional strength, and interfacial fracture energy can be obtained using a recently proposed theoretical model.

The effect of aggregate surface area on the interfacial bond properties was studied. The geometry of the cylindrical aggregate was altered by either varying the aggregate embedded length or by varying the aggregate diameter. The interfacial stiffness, shear bond strength, and frictional bond strength remained relatively constant, because the physical and chemical composition of the interface was not altered. However, the specific surface energy showed an increase for the longer embedded lengths. This may reflect the fact that the interfacial crack propagates in a quasibrittle manner with a rising R-curve rather than in a perfectly brittle manner as was assumed in the theoretical model.

The interfacial properties were varied with the addition of several admixtures. Substantial improvements in bond properties were obtained by adding silica fume, latex, and latex with an antifoaming agent to the cement matrix. The addition of silica fume showed the largest improvements, especially in the value of bond fracture energy. The addition of fine aggregates to the cement showed no changes in bond properties and parameters. The addition of multiple coarse aggregates to the matrix produced a small decrease in the bond properties, due to the altered physical characteristics of the cement matrix with the embedded aggregates.

The interfacial zone was examined using backscattered electron imaging, and the porosity of the interface was quantified using an image analysis system. The addition of admixtures was seen to decrease the porosity of the interfacial zone; specimens containing silica fume or latex with an antifoaming agent showed the most significant decrease in porosity of the interfacial zone. The addition of fine aggregates to the cement matrix had no effect on the interfacial porosity.

A relationship between the interfacial mechanical properties and the microstructural investigation was obtained. Comparison of the bond properties and interfacial porosity gradients has shown a direct correlation. It can be shown that the microstructure of the

interface plays a substantial role in the mechanical behavior of the aggregate/cement bond.

Acknowledgment

The authors acknowledge the financial support from the National Science Foundation Center for Science and Technology of Advanced Cement Based Materials.

References

1. Diamond, S. In *Proceedings of 8th International Congress on the Chemistry of Cement, I*; Brazil, 1986; pp 122–147.
2. Monteiro, P.J.M.; Maso, J.C.; Oliver J.P. *Cem. Concr. Res.*, **1985,** *15*, 953–958.
3. Scivener, K.L.; Bentur, A.; Pratt, P.L. *Adv. Cem. Res.* **1988,** *1*, 230–237.
4. Zimbelmann, R. *Cem. Concr. Res.* **1985,** *15*, 801–808.
5. Struble, L.; Sklany, J.; Mindess, S. *Cem. Concr. Res.* **1980,** *10*, 277–286.
6. Langton, C.A.; Roy, D.M. In *Proceedings of 7th International Congress on the Chemistry of Cement, III*; USA, 1985; 127–132.
7. Zimbelman, R. *Cem. Concr. Res.* **1987,** *17*, 651–660.
8. Hillemeier, B.; Hilsdorf, H.K. *Cem. Res.* **1977,** *7*, 523–536.
9. Lyubimova, T. Yu; Pinus, E.R. *Colloid J.* **1962;** *24*, 578–587.
10. Shah, S.P.; Slate, F.O. In *International Conference on the Structure of Concrete, Paper B3*; 1968; 1–11.
11. Alfornd, N. McN.; Poole, A.B. *Cem. Concr. Res.* **1979,** *9*, 583–589.
12. Mitsui, K.; Li, Z.; Lange, D.A.; Shah, S.P. *ACI Mater. J.* **1994,** *91*, 30–39.
13. Sang, H.; Li, Z.; Shah, S.P. *J. Eng. Mech.* **1990,** *116*, 2136–2150.
14. Li, Z.; Mobasher, B.; Shah, S.P. *J. Am. Ceramic Soc.* **1991,** *74*(9), 2156–2164.
15. Ouyang, C.; Alvarez, A.P.; Shah, S.P. *J. Eng. Mech.* **1994,** *120*(12), 2641–2659.
16. Bentur, A.; Cohen, M.D. *J. Am. Ceramic Soc.* **1987,** *70*(10), 738–743.